

<https://doi.org/10.1038/s44310-025-00061-w>

# Telecom wavelength quantum dots interfaced with silicon-nitride circuits via photonic wire bonding



Ulrich Pfister<sup>1,4</sup>✉, Daniel Wendland<sup>2,3,4</sup>✉, Florian Hornung<sup>1</sup>, Lena Engel<sup>1</sup>, Hendrik Hüging<sup>2</sup>, Elias Herzog<sup>1</sup>, Ponraj Vijayan<sup>1</sup>, Raphael Joos<sup>1</sup>, Erik Jung<sup>3</sup>, Michael Jetter<sup>1</sup>, Simone L. Portalupi<sup>1</sup>, Wolfram H. P. Pernice<sup>2,3</sup> & Peter Michler<sup>1</sup>

Photonic integrated circuits find applications in classical and quantum communication, computing and sensing. For ideal performance, efforts are made to effectively combine different platforms to benefit from their respective strengths. Here, direct laser written photonic wire bonds are employed to interface triggered sources of quantum light, based on semiconductor quantum dots embedded into etched microlenses, with low-loss silicon-nitride photonics. Single photons at telecom wavelengths are generated by In(Ga)As quantum dots which are then funneled into a silicon-nitride chip containing single-mode waveguides and beamsplitters. The second-order correlation function of  $g^{(2)}(0) = 0.11 \pm 0.02$ , measured via the on-chip beamsplitter, clearly demonstrates the transfer of single photons into the silicon-nitride platform. The photonic wire bonds funnel on average  $27.9 \pm 8.0\%$  of the bare microlens emission (NA = 0.6) into the silicon-nitride-based photonic integrated circuit even at cryogenic temperatures. This opens the route for the effective future up-scaling of circuitry complexity based on the use of multiple different platforms.

For modern quantum technologies, the transfer from large bulk optics experiments<sup>1,2</sup> to scalable photonic chips with several optical elements is highly desirable<sup>3</sup>. Indeed, several implementations in quantum communication<sup>4</sup>, optical quantum computing<sup>5</sup>, simulation<sup>6</sup>, and sensing<sup>7</sup> can strongly benefit from the possibility to increase the experimental complexity still on a small footprint device. In 2001, an efficient photonic quantum computation scheme was proposed by using only linear optics elements, single-photon sources, beamsplitters, phase shifters, and photodetectors<sup>8</sup>. This stimulated the search for a platform capable of including all these elements simultaneously, ideally providing state-of-the-art performance for each component. Silicon (Si) and silicon-nitride (Si<sub>3</sub>N<sub>4</sub>) showed that large-scale photonic integrated circuits can be realized, thanks to the achievable low losses in light propagation<sup>3</sup>. For the generation of quantum light, spontaneous four-wave mixing or spontaneous parametric down-conversion have been used in exciting experiments<sup>9–11</sup>. Nevertheless, the probabilistic nature of the light emission process can impact the further upscaling of the experimental complexity. This is where deterministic sources of quantum light, as for example semiconductor quantum dots (QDs), can play a key role<sup>12</sup>. In 2018, the simultaneous operation of a III-V

chip with QDs as single-photon source, single-mode waveguides (WGs), a 50:50 beamsplitter and two single-photon detectors was demonstrated<sup>13</sup>. Still, the high losses observed in the photonic circuitry represent a challenge in reaching the same photonic complexity as achieved in Si and related material systems. Therefore, it seems advantageous to combine these platforms in order to benefit from each other's key strengths using a hybrid interface<sup>14</sup>. There already exist several approaches including wafer bonding<sup>15–17</sup>, transfer printing<sup>18,19</sup> and pick and place techniques<sup>20,21</sup>, combining the advantages of different platforms. For well established photonic integrated circuits (PICs) on low-loss platforms, 3D direct laser writing (DLW)<sup>22–26</sup> offers a high design flexibility to fabricated photonic elements on a micrometer scale providing versatile solutions for individual challenges. This flexibility has been already demonstrated via laser-written photonic wire bonds (PWB)<sup>27</sup> that allowed to guide laser emission into a PIC<sup>28</sup>, a connection of two silicon-on-insulator PICs<sup>29</sup> and recently the guiding of single-photons from QDs emitting in the near-infrared, embedded in monolithically etched WGs, into a fiber array<sup>30</sup>. In this work, PWBs are employed to form an interface between the III-V platform and the Si<sub>3</sub>N<sub>4</sub>-based PIC for an on-chip beamsplitting, as schematically shown in Fig. 1.

<sup>1</sup>Institut für Halbleitertechnik und Funktionelle Grenzflächen, Center for Integrated Quantum Science and Technology (IQST) and SCoPE, University of Stuttgart, Allmandring 3, 70569 Stuttgart, Germany. <sup>2</sup>Institute of Physics and Center for Nanotechnology, University of Münster, 48149 Münster, Germany. <sup>3</sup>Kirchhoff-Institute for Physics, University of Heidelberg, 69120 Heidelberg, Germany. <sup>4</sup>These authors contributed equally: Ulrich Pfister, Daniel Wendland.

✉ e-mail: [ulrich.pfister@ihfg.uni-stuttgart.de](mailto:ulrich.pfister@ihfg.uni-stuttgart.de); [daniel.wendland@uni-muenster.de](mailto:daniel.wendland@uni-muenster.de)

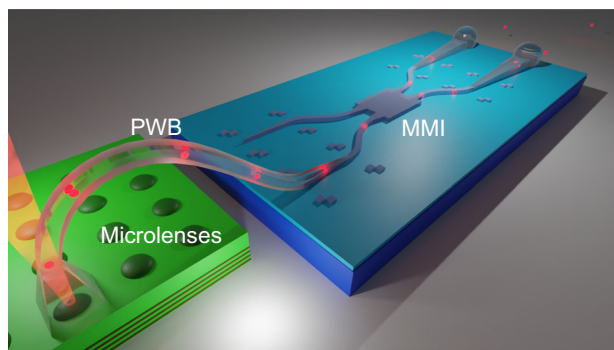


**Fig. 1 | Sketch of the hybrid photonic chip.** On the left (in green), the InAs/GaAs platform is shown with the AlAs/GaAs DBRs and the microlenses above the quantum dot layer. On the right (in blue), the  $\text{Si}_3\text{N}_4$ -based platform with the corresponding fabricated beamsplitter is depicted. Both platforms are connected by the laser written photonic wire bonds. The top excitation of the QDs is also visualized.

Indium gallium arsenide (In(Ga)As) QDs are used as single-photon sources emitting at telecom-wavelengths in combination with truncated Gaussian-shaped microlenses for a more Gaussian-like emission profile.

## Results

### Device fabrication

The sample containing the QDs was grown on a GaAs substrate via metal-organic vapor-phase epitaxy. It consists of a distributed Bragg reflector (DBR) formed by 23 AlAs/GaAs pairs acting as a bottom mirror to reduce losses into the substrate. Subsequently, an InGaAs metamorphic buffer (MMB)<sup>31</sup> was used, acting as a strain relaxation layer for engineering the emission wavelength to the C-/S-band. Next, the In(Ga)As QD layer followed and was capped afterwards by a 805 nm thick InGaAs layer which is needed for the successive fabrication of the microlenses. As preliminary step for the employed  $\text{SiO}_2$  etch mask for the microlens fabrication, a native oxide-removal step was conducted to increase the adhesion to the InGaAs surface and the resists were afterwards spin-coated. A mask aligner was used to expose the resist layers via a hard-mask lithography with a single exposure step. After the development of the resists, 50 nm of  $\text{SiO}_2$  were applied to the sample surface employing electron-beam evaporation. The necessary heating for this fabrication step altered the spectra of the employed QDs emitting in the telecom C-/S-band. This made a deterministic microlens positioning, as performed in a previous work with QDs emitting in the telecom O-band<sup>32</sup>, not directly feasible here. This issue is in the focus of current research by optimizing the epitaxial growth to achieve a higher temperature resistance of the QDs. In a last step, the wet chemical etching was performed with an etching solution ratio of  $\text{H}_2\text{SO}_4:\text{H}_2\text{O}_2:\text{H}_2\text{O}$  of 1000:1:200 at a constant temperature of 80° C. Using FDTD, the target dimensions of the microlens with a diameter of 2.2  $\mu\text{m}$ , lens height of 350 nm and a distance of 400 nm from the QD layer to the microlens baseline, were determined for optimum performance. After the wet chemical etching, atomic force microscopy measurements were performed to identify a region close to these ideal parameters. Once this region was located, the sample was cleaved to ensure that the microlenses were found close to the chip edge. In this way, the distance between the III-V sample and the  $\text{Si}_3\text{N}_4$ -based PIC is minimized. This reduces the necessary PWB printing length, improving the mechanical stability as well as the propagation losses. Before the actual printing, the array of lenses was pre-characterized with a free-space micro-photoluminescence setup employing an objective with a numerical aperture (NA) of 0.6 to identify suitable candidates for the PWB. This allows to compare the behavior of the non-deterministically positioned microlenses before and after the 3D printing, being particularly important for the reliable quantification of the efficiency of the approach. The initial characterization of the etched microlenses was performed in a helium-flow cryostat at 4 K with a confocal setup configuration. All microlenses in the relevant region were investigated and the corresponding spectra of the QDs

were measured under above-band (AB) excitation in saturation with a continuous wave laser at 800 nm. In total, 52 suitable candidates were found and 47 of them showed sufficient separation. Next, the  $\text{Si}_3\text{N}_4$ -based PIC was designed according to the positions of the pre-selected microlenses. This was done with the help of the open-source python-based framework *gdsheplers*<sup>33</sup>. The integrated structures were designed so that their positions match those of the pre-characterized lenses. For the fabrication of the PIC, a 525  $\mu\text{m}$  thick Si handle wafer with a 3.3  $\mu\text{m}$   $\text{SiO}_2$  buffer layer and 330 nm of stoichiometric low pressure chemical vapor deposited (LPCVD)  $\text{Si}_3\text{N}_4$  was used. Since the III-V sample embedding the QDs had an overall thickness of 380  $\mu\text{m}$ , the  $\text{Si}_3\text{N}_4$  chip was polished to reduce the bottom Si substrate to an overall thickness close to the III-V sample. This was done to reduce the necessary upwards and downwards bends in the bridging PWBs. In a next step, the PIC design was transferred on to the  $\text{Si}_3\text{N}_4$  layer, using a negative tone resist, spin coating and electron beam lithography. Consecutively executed reactive ion etching formed the PIC in the  $\text{Si}_3\text{N}_4$  layer. The PIC includes multi-mode interference (MMI) couplers with two input and two output WGs ( $2 \times 2$ ) as shown in the inset in Fig. 2a). The input WGs are routed to the edge facing to the QD sample, while the output WGs are spanning over the rest of the PIC sample towards the detection setup. To reduce the distance between the WG ends and the edges of the  $\text{Si}_3\text{N}_4$  sample as much as possible, considering the dimensions of the DLW structures, a subsequent dicing step was performed. After finishing the individual fabrication of the III-V and  $\text{Si}_3\text{N}_4$  samples, both were manually aligned to each other on top of a silicon-carbide (SiC) carrier. A proper alignment was achieved by using etched markers in the  $\text{Si}_3\text{N}_4$  layer as reference positions and by backside illumination through the SiC a UV-curable adhesive secured the positioning. A subsequent development, using PGMEA (propylene glycol methyl ether acetate), removed excess adhesive that might have ended up on top of the samples.

In a last fabrication step the PWBs were created, connecting the III-V platform with the  $\text{Si}_3\text{N}_4$ -based PIC. Additionally, the lensed side couplers at the outputs of the PIC were fabricated. The latter, shown in Fig. 2b), are suitable to enhance the coupling efficiencies in the given off-chip detection configuration. They were the first 3D components fabricated due to their higher mechanical stability compared to the PWBs. For this a Nanoscribe GT system was used in combination with the high refractive index polymer IP-n162 ( $n > 1.59$  at 1550 nm). By alignment through image detection onto etched markers, schematically shown in Fig. 1, the side couplers were positioned on the WG ends. They increase the WG mode by using a taper, which increases linearly over 230  $\mu\text{m}$  from a square cross section with a side length of 1.5  $\mu\text{m}$  to 14  $\mu\text{m}$ . The enlarged mode is met by a spherical lens with a radius of 28  $\mu\text{m}$ , to compensate the divergence of the outcoupled beam. After a subsequent development, the sample-system was again mounted in a Nanoscribe GT system for the fabrication of the PWBs. They are created from the polymer IP-Dip and aligned towards the integrated  $\text{Si}_3\text{N}_4$  photonics by using the same marker detection as mentioned before. An overview of the PWB structure can be seen in Fig. 2c). To couple the light from the PWBs into the WGs, a mode converter, as already presented similarly<sup>34</sup>, is used. It consists of an inverse tapered  $\text{Si}_3\text{N}_4$  section, that is embedded in a rectangular polymer WG of constant width, and increasing height. To avoid printing artefacts at the rough edge of the  $\text{Si}_3\text{N}_4$  sample due to the dicing process, the PWBs were lifted before they reach the edge of the sample. After a bend towards the QD sample, the PWBs are tapered from their original cross section of  $2 \times 2 \mu\text{m}^2$  to  $3 \times 3 \mu\text{m}^2$  to enhance the mechanical stability. The development of the PWBs was performed with PGMEA and isopropanol, with an additional step of Novec<sup>TM</sup> (Sigma-Aldrich SHH0002) to avoid the necessity of blow drying the sample. The mechanical stability and functionality of the fabricated PWBs were investigated and optimized in previous test samples, as often detached PWBs were visible. Therefore, the adhesion was improved by adding the previously mentioned tapered region and ensuring a full exposure of the resist in contact to the III-V surface. For testing this improved processing, the microlens emission was funneled into straight WGs without additional MMIs (not shown), demonstrating successful operation at cryogenic temperatures. After several cooling cycles,

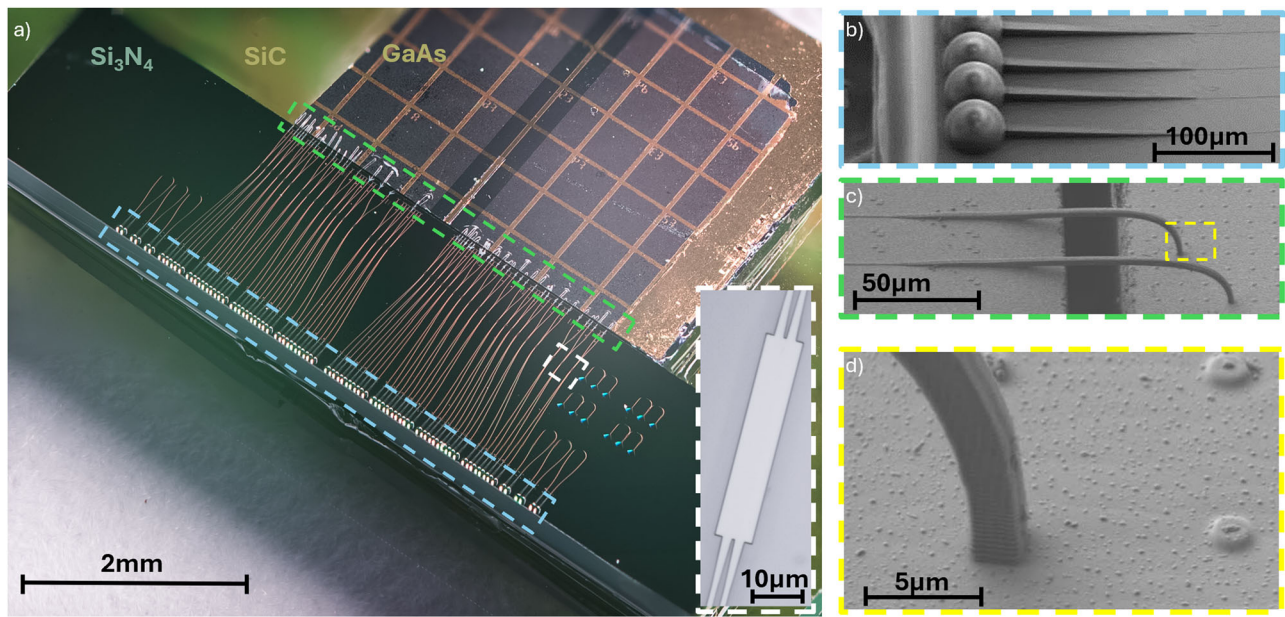


**Fig. 2 | Sample overview.** **a** The photograph shows the fully assembled hybrid system, consisting of the In(Ga)As/GaAs QD sample, which is aligned to a PIC sample made from  $\text{Si}_3\text{N}_4$ . The aligned samples are glued to a SiC carrier chip. In the inset, a microscope picture of the fabricated MMIs can be seen. **b** The scanning electron micrograph shows the side couplers that couple the light from the chip to the collection objective. They are fabricated using DLW, and consist of a linear taper

and a spherical lens. **c** Photonic wire bonds bridge the gap of roughly  $30\ \mu\text{m}$  between both samples. On the left the PIC sample can be seen with WGs and alignment markers made from  $\text{Si}_3\text{N}_4$ . **d** The highlighted area from **c** is shown as a close up. On the right two microlenses can be seen that have not been contacted, while on the left the interface of a PWB and a microlens is shown.

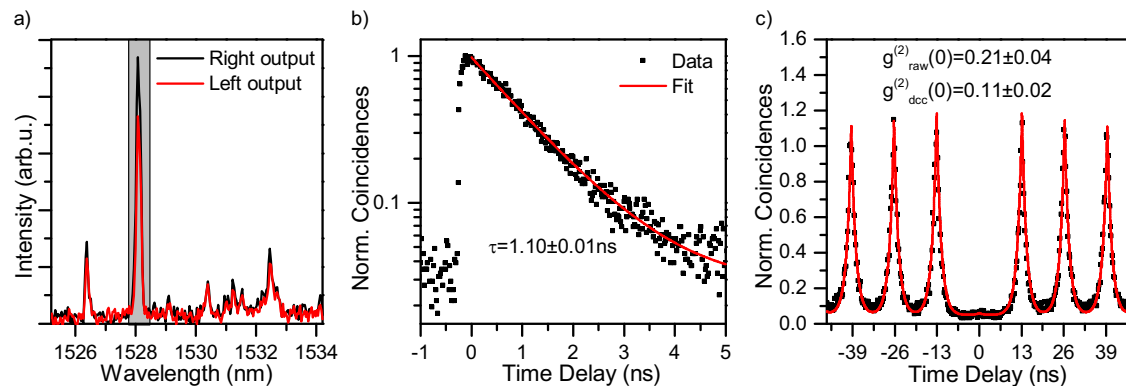


**Fig. 3 | Optical characterization.** **a** Measured spectra of both beamsplitter output ports of the investigated QD using the same spectrometer entrance and integration time. The highlighted area in gray indicates the investigated transition. **b** Decay time measurement of the investigated transition at  $1528.1\ \text{nm}$  under weak pulsed AB excitation. **c** Second-order correlation measurement under pulsed AB excitation at

saturation power with a binwidth of  $250\ \text{ps}$ . The  $g_{\text{raw}}^{(2)}(0)$  was determined by comparing the integrated coincidences in a  $13.14\ \text{ns}$  window around the zero-delay peak and the average coincidences in the same window around a peak in the Poissonian level.  $g_{\text{dcc}}^{(2)}(0)$  is the value corrected for the additional coincidences due to the SNSPD dark counts.

many of the fabricated PWBs did not show damages or detachment. This allowed the realization of the device shown in Fig. 2, which brought the results discussed in the next section.

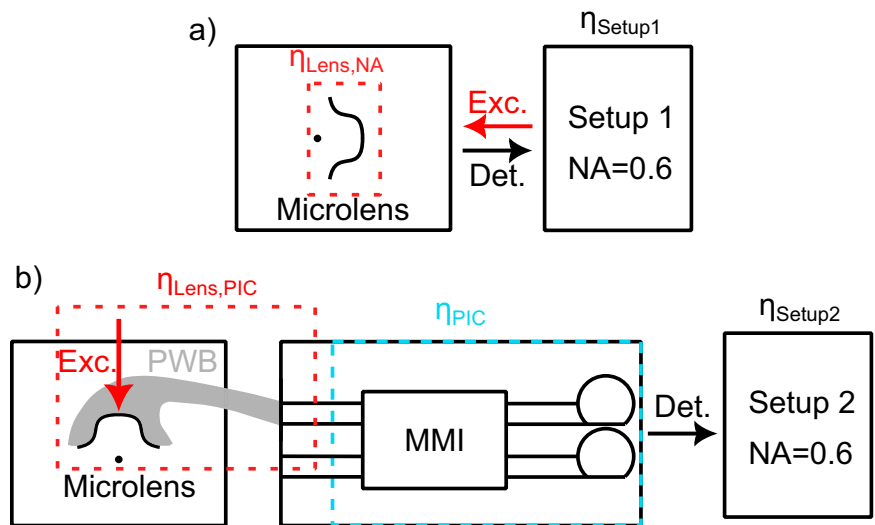
## Experimental results

The fully assembled sample-system was mounted in a helium-flow cryostat allowing the excitation from the top and the simultaneous collection of the horizontal emission from the side couplers, as schematically shown in Fig. 1. For the collection of the emitted light, both output ports of the MMI were used with the help of an objective with a NA of 0.6. Both emission paths were spatially separated by a  $4f$  setup and afterwards coupled into single-mode fibers. Several structures suitable for further experiments with a splitting ratio (SR) close to 50:50 (R:T) were found. For multiple of these structures, the emission spectrum showed different transition lines compared to the

bare pre-selected microlenses. This behavior is attributed to non-ideal collection condition due to the non-deterministic microlens positioning, together with the spatially wide collection window of the  $3\ \mu\text{m}$  broad PWB interface. This allows nearby QDs emission to couple and may change the collected spectra. This issue can be reduced in the future when deterministic fabrication is employed and the centered QD dominates the present emission. Furthermore, a slight blue shift ( $\approx 0.84\ \text{meV}$ ) was also observed on the pre-selected lines which is attributed to the induced strain by the DLW structures during the cooling down as well as to the changed excitation conditions due to the presence of the PWB structures<sup>35</sup>. In the following, one of the investigated structures showing stable emission over several cooling cycles is investigated in more detail. This structure shows a SR of  $(57.5:42.5) \pm 1.2\ \%$ , both detected output spectra are shown in Fig. 3a). The QD displays a main transition line, attributed to a trion, at  $1528.1\ \text{nm}$ . This



**Fig. 4 | Schematic illustration of the different measurement configurations highlighting all included efficiencies  $\eta$  in Eq. (1).** **a** Setup 1 used for the pre-selection of the microlenses allowing a confocal excitation and detection. **b** Setup 2 used for the investigation of the fully assembled hybrid chip enabling orthogonal excitation and detection at the same time.



transition was excited using weak AB excitation at 800 nm with a 76 MHz excitation rate. The emission was then spectrally filtered using a tunable fiber-coupled bandpass filter with a full width at half maximum of 0.5 nm and time-correlated single-photon counting was performed. The measured decay time  $\tau$  in Fig. 3b) corresponds to  $1.10 \pm 0.01$  ns, which is in the expected range for QDs grown on a MMB<sup>31,36</sup>. To demonstrate that single-photons were successfully coupled from the III-V sample to the Si<sub>3</sub>N<sub>4</sub>-based PIC, both MMI outputs were filtered and detected simultaneously. The MMI is used as a beamsplitter in a Hanbury Brown and Twiss interferometer, allowing to obtain the second-order correlation function by detecting the single-photons with superconducting nanowire single-photon detectors (SNSPDs). Under pulsed AB excitation in saturation, a nearly vanishing center peak in Fig. 3c) proves single-photon operation. The data analysis shows an integrated value of  $g_{\text{raw}}^{(2)}(0) = 0.21 \pm 0.04$  for a time window of 13.14 ns. The uncorrelated background caused by the SNSPD dark counts of 300 Hz can be corrected, resulting in  $g_{\text{dec}}^{(2)}(0) = 0.11 \pm 0.02$ . The non-vanishing contribution in the  $g^{(2)}(0)$  is attributed to residual uncorrelated background emission due to the utilized AB excitation. In the future, this could be improved by using quasi-resonant or resonant excitation schemes, like p-shell excitation or the SUPER scheme<sup>37</sup>. From the blinking behavior<sup>38</sup>, an optical on-time of  $\beta_{\text{on}} = 80.00 \pm 0.01$  % was estimated. The measurements were performed with a dark count subtracted count rate of  $\approx 4600$  counts per second and per output, corresponding to an overall efficiency of  $\eta_{\text{Total}} = 0.012$  %. This is comparable to another PWB related work with QDs as single-photon source<sup>30</sup>. The overall efficiency is here strongly limited by the microlens, which provides a more Gaussian-like emission profile according to simulations, but showed experimentally no increase in the extraction efficiency compared to planar samples with a weak  $\lambda$ -cavity between bottom DBR and the semiconductor-vacuum interface.

### Interface performance

The successful transfer of single-photons into the PIC has been demonstrated and the efficiency of the hybrid approach was further analyzed. Particularly the PWB efficiency plays a fundamental role for the presented hybrid approach. A direct efficiency measurement of the PWB transmission was not feasible since the microlenses on the III-V sample also have to be considered in the transmission definition. Therefore, the ratio  $\Gamma_{\text{trans}}$  between the lens to PIC transmission efficiency  $\eta_{\text{Lens,PIC}}$  and the detection efficiency  $\eta_{\text{Lens,NA}}$  of the bare microlenses using an NA of 0.6 is quantified by isolating both values via

$$\Gamma_{\text{trans}} = \frac{\eta_{\text{Lens,PIC}}}{\eta_{\text{Lens,NA}}} = \frac{\overline{I_{\text{PIC}}} / (\eta_{\text{PIC}} \eta_{\text{Setup2}})}{\overline{I_{\text{Lens}}} / \eta_{\text{Setup1}}} \quad (1)$$

For the comparison, the average intensity of 9 working PWB structures  $\overline{I_{\text{PIC}}}$  and of the 52 pre-selected bare microlenses  $\overline{I_{\text{Lens}}}$  are determined by summing up the measured spectra. This has the advantage of taking several working structures into account, providing a more precise estimation of the general performance of the presented approach. Different measurement configurations were used due to the varying excitation and detection geometries and therefore have to be taken into account, as schematically shown in Fig. 4. The efficiency of the used setups were measured, corresponding to  $\eta_{\text{Setup1}} = 40.1 \pm 0.6$  % for the pre-selection and  $\eta_{\text{Setup2}} = 37.9 \pm 0.3$  % for the hybrid approach. For the latter also the PIC efficiency  $\eta_{\text{PIC}}$  has to be considered. The losses directly related to the Si<sub>3</sub>N<sub>4</sub>-based PIC elements can be measured individually and are only minimal, with  $98.0 \pm 0.1$  % transmission efficiency for the full WG length and additional  $94.8 \pm 1.6$  % for the MMIs. More dominant are the side coupler losses, caused by the mode-converter section, internal reflections at the polymer to air interface and a slight mode mismatch reducing the achievable fiber coupling, resulting in an efficiency of  $67.6 \pm 1.7$  %. Overall, the PIC shows a total transmission of  $\eta_{\text{PIC}} = 62.8 \pm 2.7$  %, measured at room temperature conditions for 1550 nm. Inserting all values in Eq. (1) to isolate  $\eta_{\text{Lens,NA}}$  and  $\eta_{\text{Lens,PIC}}$  results in a transfer ratio of  $\Gamma_{\text{trans}} = 27.9 \pm 8.0$  % for the microlens to PIC interface compared to the bare microlens in combination with an objective with a NA of 0.6. It can be seen that the amount of transferred photons is clearly smaller than the one measured for the bare microlenses. We note that a higher collection efficiency at the PWB to microlens interface is expected due to the spatially wide collection range compared to the limited NA of the employed objective. The nevertheless reduced transmission efficiency can be attributed to the bending and DLW imperfection of the PWBs, introducing losses on the guided signal. The dimensions of the PWBs, in terms of length and diameter, also introduce additional losses. The necessary printing distance of  $\approx 200$   $\mu\text{m}$  and the different expansion coefficients of the material platforms increases the mechanical stress during the cooling process. The diameter of the PWBs ( $2 \times 2$   $\mu\text{m}^2$ ) is large enough to support multiple modes and was chosen for mechanical stability rather than for optical reasons. While this in principle allows a more efficient collection of the light emitted by the QDs, it reduces the overlap to the single-mode Si<sub>3</sub>N<sub>4</sub> WGs. Especially the discrimination of TM components should suppress the efficiency significantly as it is to be expected that the QDs emission couples more or less uniformly in TE and TM components in AB excitation. Thus, an increased efficiency is achievable in future samples using polarization sensitive WGs. Also artifacts, stemming from standing waves which occur at the III-V surface due to the high reflectivity, as reported already<sup>39</sup>, may lead to additional losses. Nevertheless, since the surface roughness is only increased locally, no significantly increased losses are expected. The employed non-deterministic fabrication also has to be

considered. The performed pre-selection was used to increase the number of usable candidates, but the exact position of the QDs under the microlenses is still unknown. This potentially reduces the achieved extraction efficiency, since the highest photon extraction enhancement and most Gaussian-like profile is expected for QDs centrally positioned under the microlenses. This issue can be addressed by optimizing the epitaxial growth to make the QDs more stable during high temperature processes required for the microlens fabrication. This would allow the realization of a deterministic microlens positioning to enhance the extraction efficiency. In summary, the presented approach emphasizes the high flexibility of the DLW technology, but for future projects several options are available to increase the transfer and the overall efficiency even further.

## Discussion

In conclusion, single-photons from In(Ga)As QDs were successfully funneled into a Si<sub>3</sub>N<sub>4</sub>-based PIC by employing two-photon polymerization to create PWBs connecting both platforms. Truncated Gaussian-shaped microlenses were used to achieve a more Gaussian-like emission profile to increase the coupling efficiency into the PWB. For the PWBs an average transfer ratio of  $\Gamma_{\text{trans}} = 27.9 \pm 8.0\%$  directly into the Si<sub>3</sub>N<sub>4</sub>-based PIC was determined in comparison to the bare microlenses employing a NA of 0.6. The photons were guided into a beamsplitter forming a Hanbury Brown and Twiss interferometer and a dark count corrected  $g_{\text{dec}}^{(2)}(0)$  of  $0.11 \pm 0.02$  was measured. This proves the effective realization of a hybrid PIC with a III-V-based single-photon source and Si<sub>3</sub>N<sub>4</sub>-based photonics. For further experiments, other excitation schemes like p-shell excitation, phonon assisted excitation or the SUPER scheme<sup>37</sup>, which has been already demonstrated for the investigated kind of QDs<sup>40</sup>, can be used to approach a higher single-photon purity. The overall efficiency from the QDs to the Si<sub>3</sub>N<sub>4</sub> circuitry could be increased by further optimizing the PWBs in terms of surface roughness as well as the coupling to the integrated WGs. In simulations, a non symmetric PWB design showed reduced coupling losses into the Si<sub>3</sub>N<sub>4</sub> WG for single-mode inputs. Nevertheless, due to the focus on the stability of the PWBs and the not single-mode like QD emission, only established  $2 \times 2 \mu\text{m}^2$  PWBs were used. The overall brightness can be improved by implementing other surface emitting architectures like circular Bragg gratings for an enhanced extraction efficiency and a Purcell enhancement of the QD emission<sup>41</sup>. Additionally, the device efficiency can be enhanced by reducing the necessary bending, which can be achieved by replacing the microlens assisted QDs with well established III-V based ridge WGs, as it has been demonstrated with In(Ga)As QDs operating at  $900 \text{ nm}$ <sup>42</sup> and with droplet etched GaAs QDs emitting at around  $780 \text{ nm}$ <sup>43</sup>. The proof-of-principle measurements in this work show a method to combine the III-V platform with the highly appealing Si<sub>3</sub>N<sub>4</sub> platform via the DLW technology. This can be used in the future to design more complex systems with an increased amount of optical elements being integrated on chip, like filters<sup>44</sup>, modulators and on-chip detectors<sup>45</sup>.

## Data availability

All data needed to evaluate the conclusions in the paper are present in the main text. Raw data are available from authors upon reasonable request.

Received: 8 November 2024; Accepted: 2 February 2025;

Published online: 17 March 2025

## References

- O'Brien, J. L., Pryde, G. J., White, A. G., Ralph, T. C. & Branning, D. Demonstration of an all-optical quantum controlled-not gate. *Nature* **426**, 264–267 (2003).
- Zhong, H.-S. et al. Quantum computational advantage using photons. *Science* **370**, 1460–1463 (2020).
- Wang, J., Sciarino, F., Laing, A. & Thompson, M. G. Integrated photonic quantum technologies. *Nat. Photonics* **14**, 273–284 (2020).
- Lo, H. K., Curty, M. & Tamaki, K. Secure quantum key distribution. *Nat. Photonics* **8**, 595–604 (2014).
- Maring, N. et al. A versatile single-photon-based quantum computing platform. *Nat. Photonics* **18**, 603–609 (2024).
- Somhorst, F. H. et al. Quantum simulation of thermodynamics in an integrated quantum photonic processor. *Nat. Commun.* **14**, 3895 (2023).
- Stokowski, H. S. et al. Integrated quantum optical phase sensor in thin film lithium niobate. *Nat. Commun.* **14**, 3355 (2023).
- Knill, E., Laflamme, R. & Milburn, G. J. A scheme for efficient quantum computation with linear optics. *Nature* **409**, 46–52 (2001).
- Spring, J. B. et al. Chip-based array of near-identical, pure, heralded single-photon sources. *Optica* **4**, 90–96 (2017).
- Kaneda, F. & Kwiat, P. G. High-efficiency single-photon generation via large-scale active time multiplexing. *Sci. Adv.* **5**, eaaw8586 (2019).
- Wang, J. et al. Multidimensional quantum entanglement with large-scale integrated optics. *Science* **360**, 285–291 (2018).
- Michler, P. & Portalupi, S. L. *Semiconductor Quantum Light Sources: Fundamentals, Technologies and Devices* (De Gruyter, 2024).
- Schwartz, M. et al. Fully on-chip single-photon hanbury-brown and twiss experiment on a monolithic semiconductor-superconductor platform. *Nano Lett.* **18**, 6892–6897 (2018).
- Elshaari, A. W., Pernice, W., Srinivasan, K., Benson, O. & Zwiller, V. Hybrid integrated quantum photonic circuits. *Nat. Photonics* **14**, 285–298 (2020).
- Davanco, M. et al. Heterogeneous integration for on-chip quantum photonic circuits with single quantum dot devices. *Nat. Commun.* **8**, 889 (2017).
- Schnauber, P. et al. Indistinguishable photons from deterministically integrated single quantum dots in heterogeneous GaAs/Si<sub>3</sub>N<sub>4</sub> quantum photonic circuits. *Nano Lett.* **19**, 7164–7172 (2019).
- Vijayan, P. et al. Growth of telecom C-band In(Ga)As quantum dots for silicon quantum photonics. *Mater. Quantum Technol.* **4**, 016301 (2024).
- Osada, A. et al. Strongly coupled single-quantum-dot-cavity system integrated on a CMOS-processed silicon photonic chip. *Phys. Rev. Appl.* **11**, 024071 (2019).
- Katsumi, R. et al. CMOS-compatible integration of telecom band InAs/InP quantum-dot single-photon sources on a Si chip using transfer printing. *Appl. Phys. Express* **16**, 012004 (2023).
- Elshaari, A. W. et al. On-chip single photon filtering and multiplexing in hybrid quantum photonic circuits. *Nat. Commun.* **8**, 379 (2017).
- Elshaari, A. W. et al. Strain-tunable quantum integrated photonics. *Nano Lett.* **18**, 7969–7976 (2018).
- Serbin, J. et al. Femtosecond laser-induced two-photon polymerization of inorganic-organic hybrid materials for applications in photonics. *Optics Lett.* **28**, 301–303 (2003).
- Guo, R. et al. Micro lens fabrication by means of femtosecond two photon photopolymerization. *Opt. Express* **14**, 810–816 (2006).
- Sartison, M. et al. 3D printed micro-optics for quantum technology: Optimised coupling of single quantum dot emission into a single-mode fibre. *Light Adv. Manuf.* **2**, 6 (2021).
- Gehring, H., Blaicher, M., Grottko, T. & Pernice, W. H. Reconfigurable nanophotonic circuitry enabled by direct-laser-writing. *IEEE J. Sel. Top. Quantum Electron.* **26**, 5 (2020).
- Preuß, J. A. et al. Low-divergence hBN single-photon source with a 3D-printed low-fluorescence elliptical polymer microlens. *Nano Lett.* **23**, 407–413 (2023).
- Schumann, M., Bückmann, T., Gruhler, N., Wegener, M. & Pernice, W. Hybrid 2D-3D optical devices for integrated optics by direct laser writing. *Light Sci. Appl.* **3**, e175 (2014).
- Billah, M. R. et al. Hybrid integration of silicon photonics circuits and InP lasers by photonic wire bonding. *Optica* **5**, 876 (2018).
- Lindenmann, N. et al. Photonic wire bonding: a novel concept for chip-scale interconnects. *Opt. Express* **20**, 17667–17677 (2012).
- De Gregorio, M. et al. Plug-and-play fiber-coupled quantum dot single-photon source via photonic wire bonding. *Adv. Quantum Technol.* **7**, 2300227 (2024).

31. Sittig, R. et al. Thin-film InGaAs metamorphic buffer for telecom C-band InAs quantum dots and optical resonators on GaAs platform. *Nanophotonics* **11**, 1109–1116 (2022).
32. Sartison, M. et al. Deterministic integration and optical characterization of telecom O-band quantum dots embedded into wet-chemically etched Gaussian-shaped microlenses. *Appl. Phys. Lett.* **113**, 032103 (2018).
33. Gehring, H., Blaicher, M., Hartmann, W. & Pernice, W. H. P. Python based open source design framework for integrated nanophotonic and superconducting circuitry with 2D-3D-hybrid integration. *OSA Contin.* **2**, 3091–3101 (2019).
34. Gehring, H., Eich, A., Schuck, C. & Pernice, W. H. P. Broadband out-of-plane coupling at visible wavelengths. *Opt. Lett.* **44**, 5089–5092 (2019).
35. Sartison, M. et al. Combining in-situ lithography with 3D printed solid immersion lenses for single quantum dot spectroscopy. *Sci. Rep.* **7**, 39916 (2017).
36. Paul, M. et al. Single-photon emission at 1.55  $\mu\text{m}$  from MOVPE-grown InAs quantum dots on InGaAs/GaAs metamorphic buffers. *Appl. Phys. Lett.* **111**, 033102 (2017).
37. Bracht, T. K. et al. Swing-up of quantum emitter population using detuned pulses. *PRX Quantum* **2**, 040354 (2021).
38. Santori, C., Pelton, M., Solomon, G., Dale, Y. & Yamamoto, Y. Triggered single photons from a quantum dot. *Phys. Rev. Lett.* **86**, 1502–1505 (2001).
39. Perez, E. F. et al. Direct-laser-written polymer nanowire waveguides for broadband single photon collection from epitaxial quantum dots into a Gaussian-like mode. *Adv. Quantum Technol.* **8**, 2300149 (2023).
40. Joos, R. et al. Coherently and incoherently pumped telecom C-band single-photon source with high brightness and indistinguishability. *Nano Lett.* **24**, 8626–8633 (2024).
41. Nawrath, C. et al. Bright source of purcell-enhanced, triggered, single photons in the telecom C-band. *Adv. Quantum Technol.* **6**, 2300111 (2023).
42. Jöns, K. D. et al. Monolithic on-chip integration of semiconductor waveguides, beamsplitters and single-photon sources. *J. Phys. D Appl. Phys.* **48**, 085101 (2015).
43. Hornung, F. et al. Highly indistinguishable single photons from droplet-etched GaAs quantum dots integrated in single-mode waveguides and beamsplitters. *Nano Lett.* **24**, 1184–1190 (2024).
44. Brücknerhoff-Plückelmann, F. et al. Broadband photonic tensor core with integrated ultra-low crosstalk wavelength multiplexers. *Nanophotonics* **11**, 4063–4072 (2022).
45. Beutel, F., Grottko, T., Wolff, M. A., Schuck, C. & Pernice, W. H. P. Cryo-compatible opto-mechanical low-voltage phase-modulator integrated with superconducting single-photon detectors. *Opt. Express* **30**, 30066–30074 (2022).

## Acknowledgements

We acknowledge the financial support of the Deutsche Forschungsgemeinschaft (DFG) via the Project 469373712, the Project GRK2642 and the CRC1459. We also thank the German Federal Ministry of

Education and Research (BMBF) for the support via Project QR.X (16KISQ013). Additionally, we acknowledge the support by the European Union's Horizon 2020 research and innovation program (grant no. 101017237, PHOENICS project). We thank Jonas Schütte for great help with the photograph in Figure 2. We acknowledge the Münster Nanofabrication Facility (MNF) for providing the tools used in the polymer and Si<sub>3</sub>N<sub>4</sub> fabrication. We warmly acknowledge the strong support of Michal Vyvlečka in scientific discussions.

## Author contributions

U.P. performed the optical and quantum optical measurements with the support of E.H., R.J. and F.H. D.W. designed and prepared the Si<sub>3</sub>N<sub>4</sub> sample and performed the 3D printing with support from E.J. D.W. and H.H. developed the side couplers. L.E. realized the microlenses, while P.V. grew the sample with the support of M.J. U.P. and D.W. wrote the manuscript with support from S.L.P. U.P. and D.W. analyzed the data. S.L.P., W.H.P. and P.M. designed the experiment and coordinated the project. All authors contributed to the revision of the manuscript and scientific discussions.

## Funding

Open Access funding enabled and organized by Projekt DEAL.

## Competing interests

The authors declare no competing interests.

## Additional information

**Correspondence** and requests for materials should be addressed to Ulrich Pfister or Daniel Wendland.

**Reprints and permissions information** is available at <http://www.nature.com/reprints>

**Publisher's note** Springer Nature remains neutral with regard to jurisdictional claims in published maps and institutional affiliations.

**Open Access** This article is licensed under a Creative Commons Attribution 4.0 International License, which permits use, sharing, adaptation, distribution and reproduction in any medium or format, as long as you give appropriate credit to the original author(s) and the source, provide a link to the Creative Commons licence, and indicate if changes were made. The images or other third party material in this article are included in the article's Creative Commons licence, unless indicated otherwise in a credit line to the material. If material is not included in the article's Creative Commons licence and your intended use is not permitted by statutory regulation or exceeds the permitted use, you will need to obtain permission directly from the copyright holder. To view a copy of this licence, visit <http://creativecommons.org/licenses/by/4.0/>.

© The Author(s) 2025